Preliminary fault analysis and paleostress evolution in the Makran Fold-and-Thrust Belt in Iran

13

A. Dolati and J.-P Burg

Keywords
Accretionary wedge • Makran • Paleostress

Introduction

The Makran is one of the largest accretionary wedges on Earth. Located in SE Iran and South Pakistan, it extends ca. 1,000 km between two, nearly N–S-running transform fault systems. To the west, the dextral Minab Fault separates the Makran subduction zone from the Zagros continent-continent collision zone (e.g. Stoecklin 1968; Bird et al. 1975). To the east, the sinistral Chaman-Ornach-Nal fault system and its offshore continuation, the Owen fracture zone, separate Makran and the Arabian plate from the Indian plate, which moves northward at 4–5 cm/a with respect to Eurasia (e.g. Paul et al. 2001; Molnar and Stock 2009; Fig. 13.1). The width of the wedge is 300–350 km from the offshore front of deformation to the depressions of Jaz Murian in Iran and Mashkel in Pakistan. More than half of the wedge is exposed on land.

Makran (MAW) is an Eocene-recent accretionary complex formed by northward convergence between the oceanic lithosphere of the Arabian plate and the Iranian Lut block and the Afghan/Helmand Block (e.g. Stoneley 1974; Jacob and Quittmeyer 1979; McCall and Kidd 1982; Zonenshain et al. 1986). The relatively large, 400–600 km gap between the trench and the volcanic arc (Fig. 13.1) was taken as an argument to contend that the subducting plate dips only 1–2° to the north. Shallow subduction is consistent with seismic data (e.g. White and Klitgord 1976; White and Louden 1982) and earthquake focal mechanisms (e.g. Jacob and Quittmeyer 1979; Byrne et al. 1992; Engdahl et al. 2006; Alinaghi et al. 2007). Seismic tomography images also a shallow slab below the Eurasian continent (Bijwaard et al. 1998; Hafkenscheid et al. 2006). Geodetic measurements indicate that the active convergence rate between Arabia and the Makran coast, measured between Mascat, in Oman, and Chabahar, on the Iranian Coast, is ca. 2 $cm.a^{-1}$ toward NNE (Fig. 13.2). The present-day convergence rate between the Makran coast (Chabahar GPS) and stable Eurasia is ca. 8 $mm.a^{-1}$ toward NNE (e.g. Vernant et al. 2004; Fig. 13.2).

In this well-constrained tectonic framework, we aimed at documenting the paleostress information that can be gained from fault plane analysis (e.g. Etchecopar et al. 1981; Angelier 1984). The coexistence of distinct brittle structures required that we clarify the chronology and the orientation of recorded stress fields across the MAW and integrate this new information in a larger regional and tectonic frame. Our primary aim was therefore to comprehend the information one can get from faults and paleostress calculation on a regional scale, in an active convergent zone. Our secondary aim was to get insight on the long-term and short-term relationships between stress and strain in seismogenic regions like Makran.

For this purpose, we combined the dynamic analysis of fault systems that define the paleostress field with that of seismic focal mechanisms that reflect the present-day stress field.

The study area covers the central part of onshore MAW in Iran (Fig. 13.1). Our work included detailed mapping with systematic measurement of fault planes. Where faults were abundant, 15–20 fault data were selected within few tens of metres to perform a reliable, computer-aided stress analysis.

The results give evidence for regional NNE–SSW compression. The calculated horizontal principal stress delineates a consistent pattern that provides the long-term, geologically established background of the seismogenic deformation in the upper levels of the MAW. Near the coast, however, recent extension dominates the brittle structures.

A. Dolati (✉) · J.-PBurg
ETH and University Zurich, Sonneggstrasse 5, CH-8092 Zurich, Switzerland
e-mail: asghar.dolati@gmail.com

A. Dolati
Geological Survey Iran, Meraj Street, Azadi Square, 13185-1494 Tehran Iran

K. Al Hosani et al. (eds.), *Lithosphere Dynamics and Sedimentary Basins: The Arabian Plate and Analogues*, Frontiers in Earth Sciences,
DOI: 10.1007/978-3-642-30609-9_13,

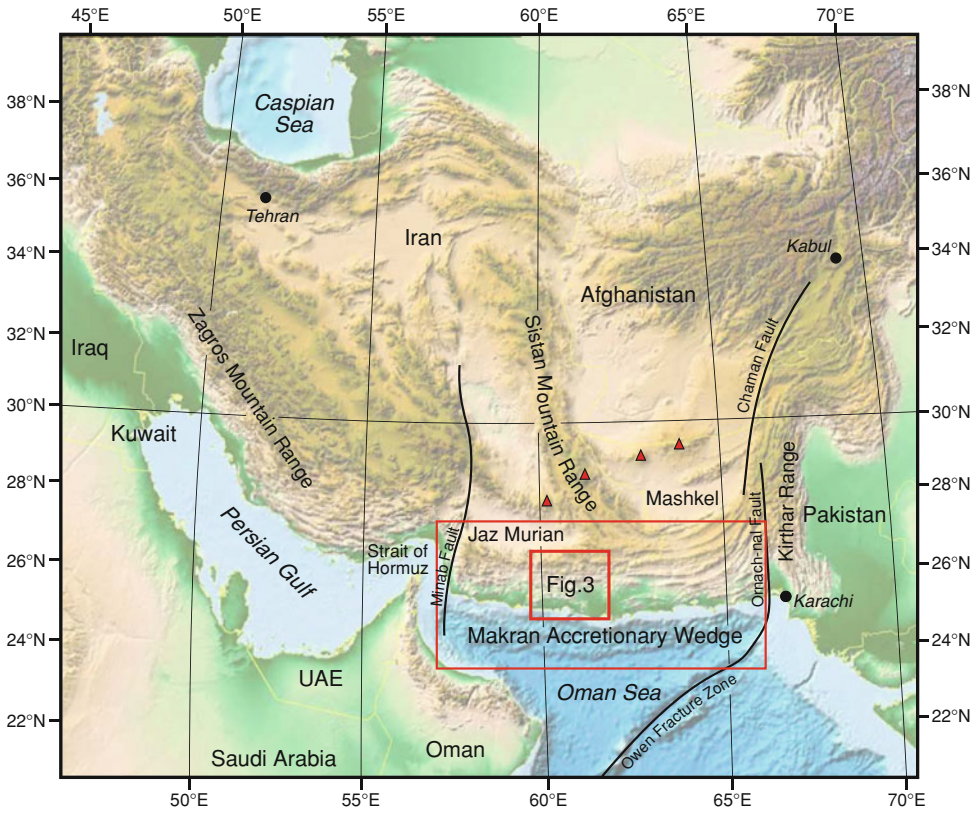

Fig. 13.1 Regional setting of the Makran accretionary complex (source map: ETOPO1, http://www.ngdc.noaa.gov/mgg/global/relief/ETOPO1/image/color_etopo1_ice_full.tif.gz). Triangles are main volcanoes of the subduction-related volcanic arc

Geological Framework

The working area was little visited since the 1970s, so that modern information documenting geological (detailed stratigraphy and kinematics) and geophysical (paleomagnetic and seismic, in particular) characteristics is lacking. Four main tectono-stratigraphic and structural units separated by major thrust zones were distinguished (Fig. 13.3). From north to south i.e. from top to bottom they are: North-, Inner-, Outer- and Coastal Makran (Dolati 2010).

North Makran, to the north of the major Bashakerd Thrust (Fig. 13.3), is dominated by Cretaceous sedimentary and igneous rocks. The complex imbricates of this zone were weakly folded around generally E-W trending axes of low-amplitude, large wavelength folds (Dolati 2010, Burg et al. this volume). Faults are mainly N–NE dipping thrusts (Fig. 13.4a). Measured fault sites were not, or by few degrees, affected by folding, which is attributed to thrust-sheet movement on flats and ramps. The NE–SW-trending part of the boundary with the Jaz Murian depression is mainly delineated by sinistral strike-slip faults (Fig. 13.4b) which cut, thus post-date folds. These faults are associated with NW–SE, conjugate dextral faults and NW–SE to N–S normal faults and reverse faults (Fig. 13.4b). The nearly E–W western part of the mapped Jaz Murian boundary is dominated by normal faults with variable orientations Fig. 13.4c.

Inner Makran, to the north of the Ghasr Ghand Thrust (Fig. 13.3), is dominated by Eocene to Lower Miocene terrigenous sandstone and shale sequences intensely folded by E–W folds (Dolati 2010, Burg et al. this volume).The Lashar, Chanf and Bamposht Thrusts are the main fault zones within Inner Makran (Fig. 13.3). Like the Ghasr Ghand thrust, they are associated with many N- to NE-dipping reverse faults and minor, conjugate S- to SW-dipping reverse faults. Deformation is typically that of a fold-and-thrust belt in which folds are controlled by flats and ramps and faulting is independent of folding (e.g. McClay 1992; Fig. 13.5). Fault measurements are consequently independent of folds and can only have been tilted by minor, late block rotations. In addition, sub-vertical (dip >80°) strike slip faults occur in many places (Fig. 13.3). Conjugate NNW–SSE dextral and NE–SW sinistral strike slip faults are particularly well developed in this unit. They suggest bulk NNE–SSW shortening. These faults cut folds and thrusts and could represent tear faults contemporaneous with shortening. Similar sets of strike slip faults cut Pliocene-Pleistocene sediments in Coastal Makran, which suggests a recent event. Outer Makran, between the Ghasr Ghand and the Chah Khan Thrusts, is dominated by Lower to Middle Miocene calcareous sandstones marls

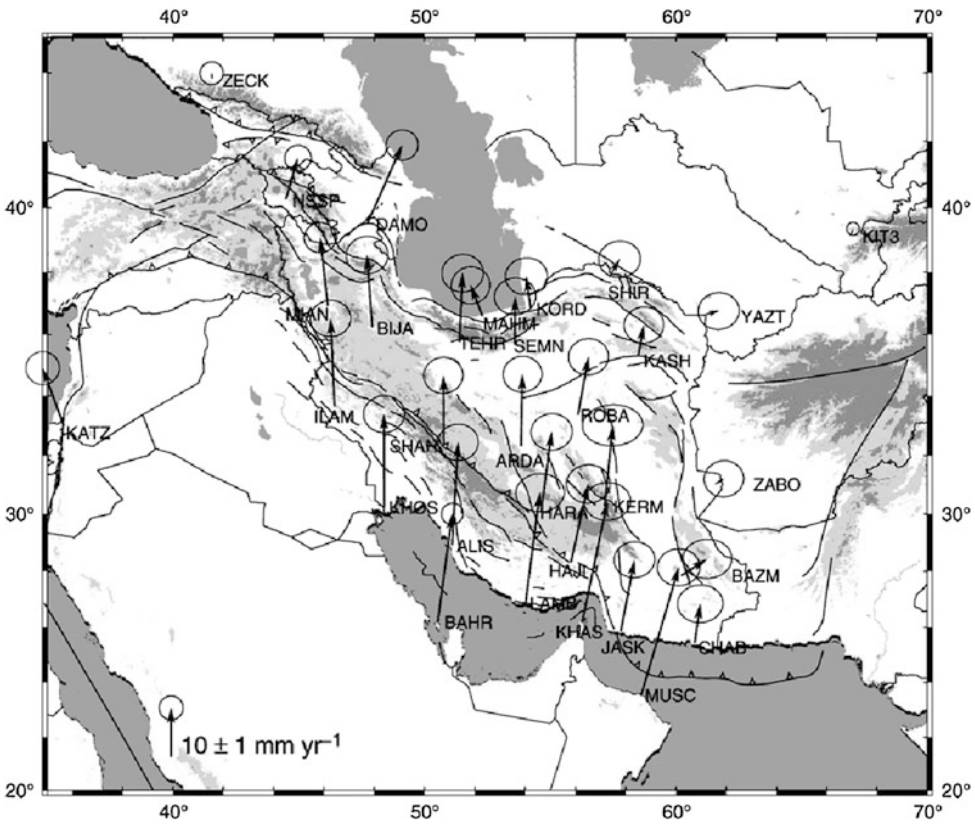

Fig. 13.2 GPS- measured, horizontal velocity of the Middle East region with respect to a fixed reference point in Eurasia (after Vernant et al. 2004)

and shales. This tectonic unit contains roughly E-W-trending open and large wavelength folds (Dolati 2010, Burg et al. this volume). Measurements of fault planes mostly document NNW- to NNE-dipping thrusts. Measured fault sites were located on <15° dipping layers, so that related, possible post-faulting rotation in fold limbs has virtually no incidence on the calculated tensor orientation. A Tortonian olistostrome is a major structural reference. It has covered unconformably some of the measured fault zones, and was later faulted in other places (Burg et al. 2008, and Fig. 13.2 in Burg et al., this volume). Accordingly, many calculated tensors in rocks older than the olistostrome are pre-Tortonian. Others are post-Tortonian. This time division will be commented in the discussion.

Coastal Makran is dominated by very weakly folded Upper Miocene sediments and faulted Pliocene to recent coastal and continental deposits. No thrust fault was observed in the studied Coastal Makran, although compressional strike slip faults were reported by (Hosseini-Barzi and Talbot 2003). Instead, normal faults cutting sediments younger than Late Miocene are general. These normal faults are usually planar and likely analogous to the normal faults cutting Pliocene-Pleistocene shelf sequences in offshore seismic sections (e.g. Cappel and Francis 1984; Platt et al. 1985; Grando and McClay 2007). Measurements of fault planes indicate two main fault sets: conjugate NNE- and SSE-dipping and W-dipping normal faults (Fig. 13.6). The number of sites was limited by the fact that the rocks are poorly consolidated, hence rarely display striations. However, the distribution of these normal fault planes suggests, as a first approximation, sub-radial extension.

Two conjugate sets of strike-slip faults occur all over the study area: they are the NE-SW-trending sinistral and NW–SE dextral faults mentioned from Inner Makran. They consistently cut and offset the major thrusts and folds and thus represent either a younger deformation event or transfer faults. The youngest strike-slip faults cut Pliocene-Pleistocene sediments of Coastal Makran and many of these faults clearly affect the topography of the MAW. Their traces are obvious on satellite images, especially where they offset resistant lithologies like sandstone (Fig. 13.7). Displacements are from a few meters up to >2,000 m. Rose diagrams and histograms of the strike-slip faults were constructed from 6,295 oriented and equal fault segments (900 m) drawn on satellite images (Fig. 13.8). The dominant set is ENE–WSW sinistral. The conjugate pattern defines NNE–SSW compression, consistent with the orientation of folds and other structures recognized throughout the MAW. Since they are very recent, no major tilt has affected these planes. Related calculated tensors were therefore expected, as they did, to yield one subvertical principal stress.

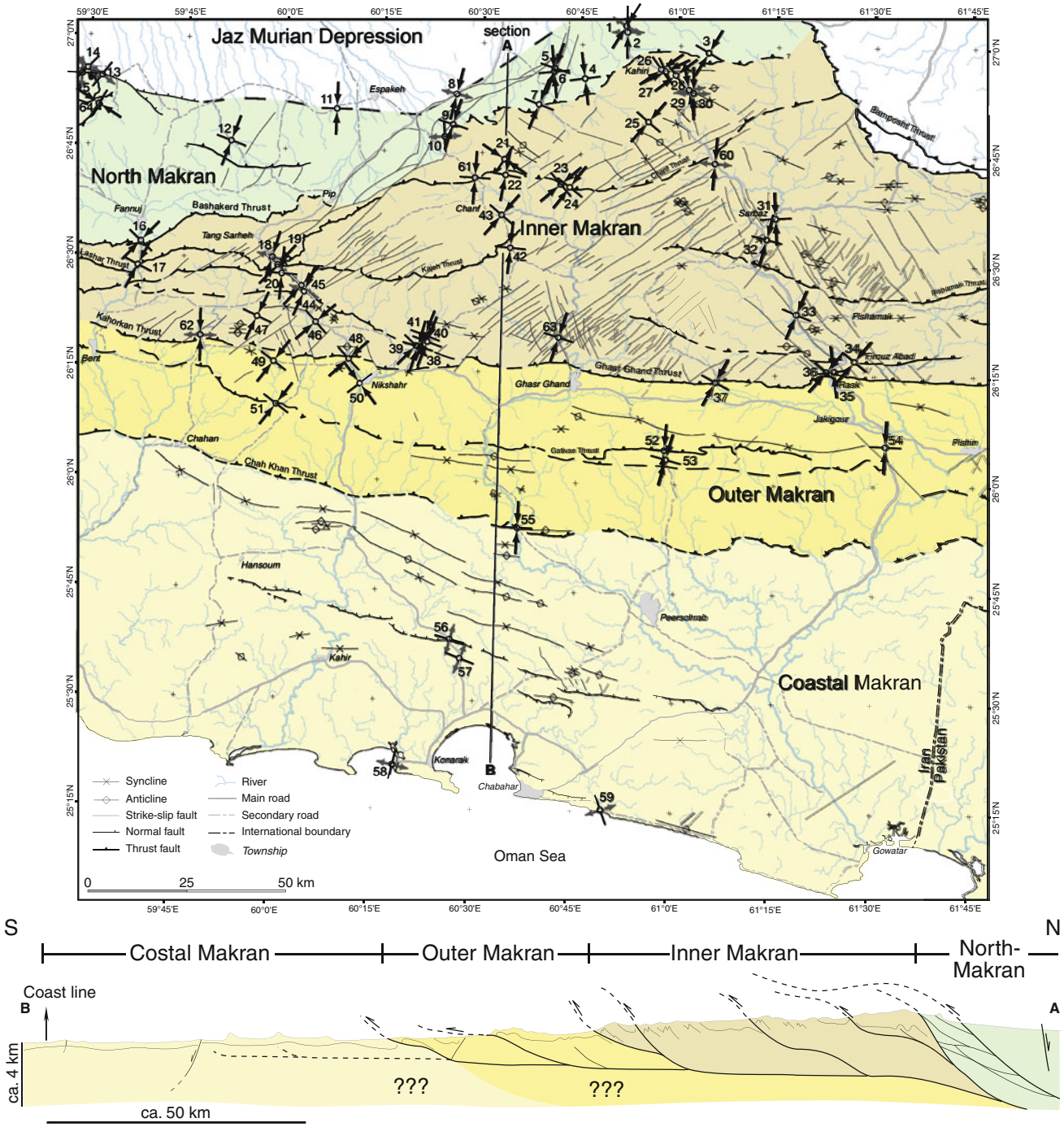

Fig. 13.3 Simplified map and synthetic section (approximate trace on map) of Central Iranian Makran (after Dolati 2010) with location of fault data

Fault and Stress Analysis

Method of Investigation and Data

The relative movement on measured fault planes was determined using classical kinematic indicators (e.g. Petit 1987), such as the growth direction of mineral fibres, which usually are calcite (Fig. 13.9). Isolated measurements were discarded, keeping 963 fault-slip data that represent 64 sites (Fig. 13.3 and Table 13.1). These sites are mainly located near major thrust zones, usually within uniform lithologies; they are usually observed over less than 200 m but over a distance sufficient to ensure a reliable kinematic analysis.

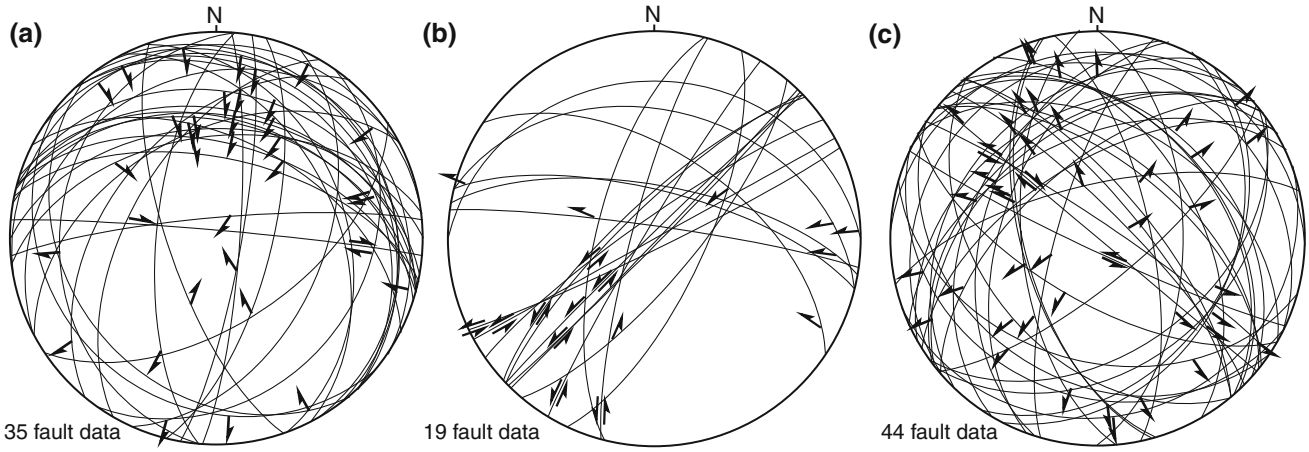

Fig. 13.4 Equal area, lower hemisphere projection of fault slip measurements out of calculated sites in North-Makran. **a** Typical association of thrusts and strike slip faults in the Bashakerd Thrust Sheet and Imbricate Zone, **b** Strike-slip-dominated system along the NE–SW contact of Jaz Murian and **c** Normal faults and strike-slip faults along the E–W contact of Jaz Murian depression. *Arrows* indicate the movement direction of the hanging wall

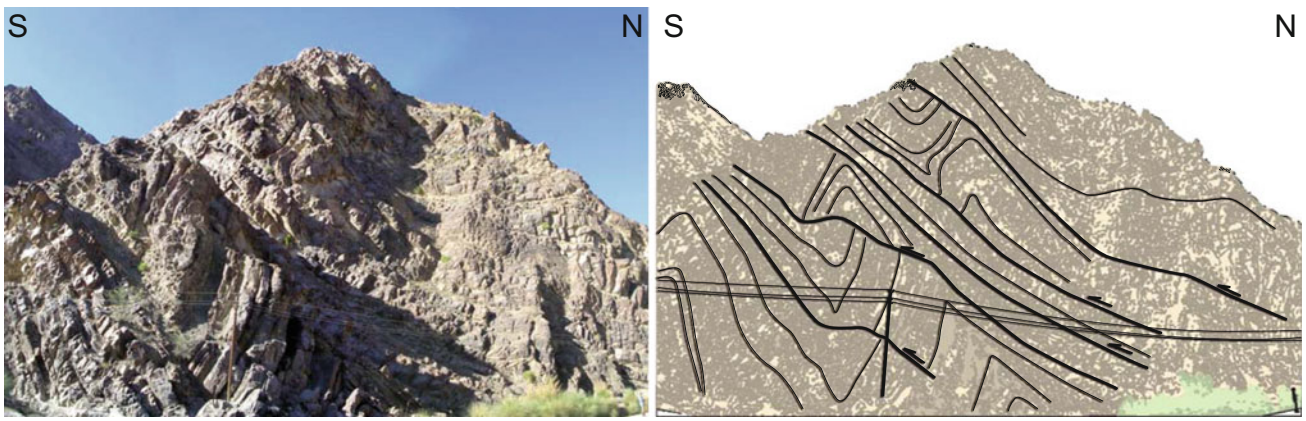

Fig. 13.5 Photo and sketch of S-vergent chevron folds involved in duplex structures and illustrating the general independence between fault planes and bedding attitude. Sandstone-dominated Upper Oligocene turbidites of Inner Makran, South of Sarbaz at 26°31′36.1″N; 61°12′20.7″E

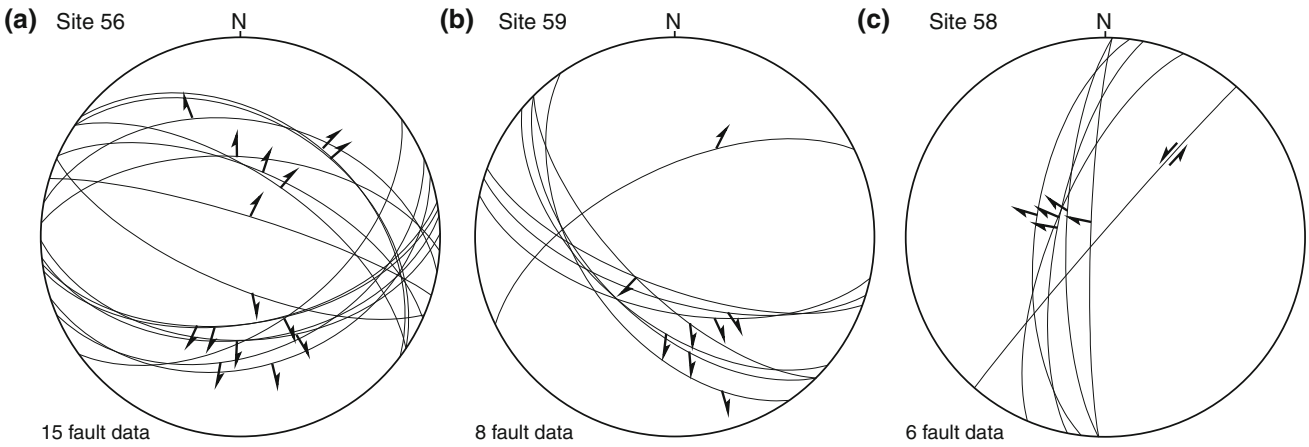

Fig. 13.6 Fault data in Coastal Makran. Measurements within 100 m around GPS points **a** 25°38′23.22″N; 60°26′27.9″E, **b** 25°15′27.5″N; 60°40′30.8″E and **c** 25°21′11.4″N; 60°18′10.0E. Site locations on Fig. 13.3. Same projection and symbols as Fig. 13.3

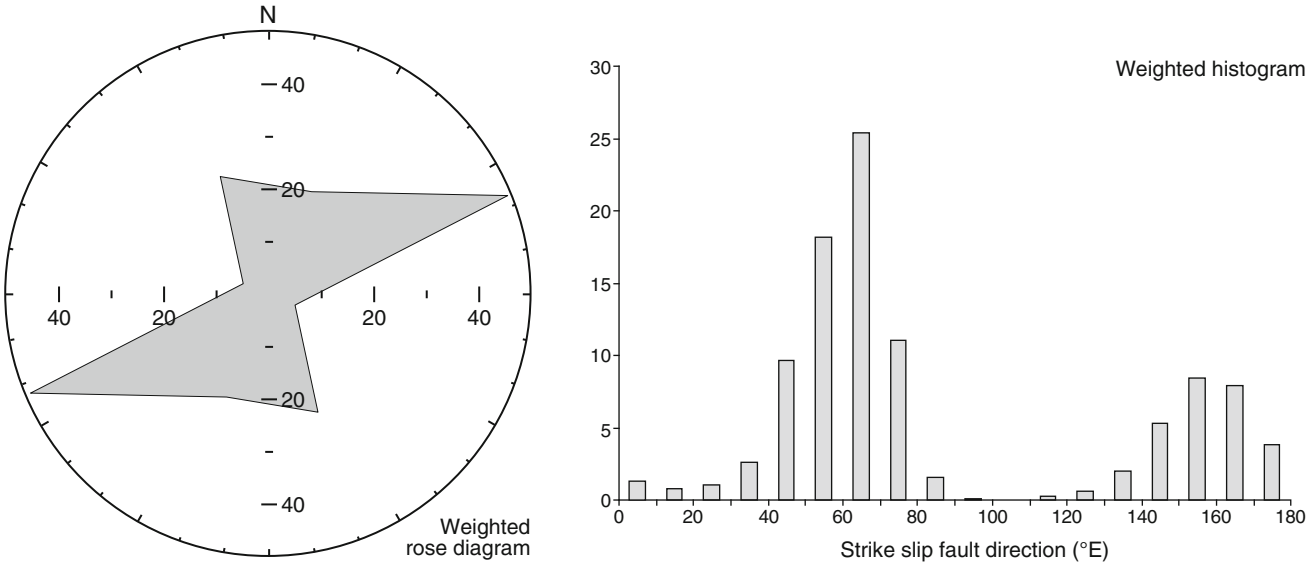

Fig. 13.8 Rose diagram (*left*) and histogram of the strike-slip faults in the study area

Fig. 13.7 Geomorphology-controlling strike-slip faults (*arrows* indicate relative, sinistral sense of movement) on the Google Earth satellite image. Latitude and longitude of central part of the picture are 26° 22′ 00″N; 60° 46′ 35″E, respectively

Fig. 13.9 Calcite fibres on a 80°, SE–dipping normal fault of the Jaz Murian boundary; GPS point: 26° 52′ 24.8″N; 60° 25′ 06.5″E

Each site comprises ten to twenty fault measurements with orientations measured as variable as possible. The rake is according to the slip direction of the hanging wall with respect to the footwall. It is measured from the strike direction and is positive counter clockwise (e.g. sinistral movement has a rake value of 180°, normal −90° and reverse +90°). We were careful in avoiding bedding-parallel striations, which indicate flexural slip during folding.

The principal stress directions, $\vec{S}_1$ (longest, compression), $\vec{S}_2$ (intermediate) and $\vec{S}_3$ (shortest, extension) were first approximated from bisecting and intersection directions of conjugate faults found in the field. This quick and simple estimate helped to control the validity of directions obtained from the computer results. Paleostress inversion methods (e.g. Etchecopar et al. 1981; Angelier 1984) rely on the assumption that shear stress is parallel to the slip direction (Wallace 1951; Bott 1959), which is in turn given by fault striations. This assumption is acceptable, except when faults closely interact (Dupin et al. 1993; Angelier. 1994).

Data processing was carried out with the Fault Slip Analysis (FSA) software of Celerier (1999) and has been described in details by Burg et al. (2005). A reduced stress tensor, with principal orientations $\vec{S}_1$, $\vec{S}_2$ and $\vec{S}_3$ with the $\vec{S}_1$ direction as close as possible to that of the measured slicken lines, was separately calculated for each locality. The magnitude ratio $r_0 = (\sigma_1 - \sigma_2)/(\sigma_1 - \sigma_3)$ characterizes the shape of the stress ellipsoid. This tensor, selected by

Table 13.1 Fault sites from the studied MAW

Lab	Longitude-E	Latitude-N	S1.az	S1.pl	S2.az	S2.pl	S3.az	S3.pl	r0	Mahaz	SV	n	Exp	Str.
1	60° 51′ 41.6″	27° 02′37.0″	26.5	48.5	43.98	−40	126.5	8.72	0.029	32	2	28	10	Cr.
2	60° 51′38.9″	27° 01′54.3″	353	35	24.41	−51	94.14	15.9	0.451	360	2	9	5	Cr.
3	61° 04′13.4″	26° 59′09.3″	220	28.3	291.2	−31	343.2	45.2	0.959	211	3	20	13	Cr.
4	60° 45′24.7″	26° 55′21.4″	174	8.37	262	−11	301.3	76.5	0.235	173	3	7	7	Cr.
5	60° 40′53.7″	26° 56′39.1″	19.7	18.1	107	−8.2	173.8	70	0.809	199	3	10	8	Cr.
6	60° 40′52.8″	26° 56′20.3″	176	0.26	265.6	−55	266.2	35	0.883	355	3	8	6	Cr.
7	60° 38′55.6″	26° 52′00.1″	202	0.43	291.5	−37	292.3	52.8	0.666	202	3	10	6	Cr.
8	60° 26′0.6′	26° 53′1.62″	193	25.1	211.8	−64	286.9	7.23	0.678	14	2	18	10	Cr.
9	60° 25′29.3	26° 48′55.4″	192	21.7	294.5	29	70.6	52.4	0.692	198	3	20	9	Cr.
10	60° 24′16.6″	26° 47′6.78″	221	52.1	350.5	26.4	93.92	25.1	0.448	357	1	20	9	Cr.
11	60° 07′43.6″	26° 50′38.0″	181	15	272.3	6.05	23.7	73.8	0.634	182	3	10	1	Cr.
12	59° 51′47.3″	26° 46′01.2″	20.2	10.8	112.2	10.1	244.4	75.1	0.556	201	3	9	6	Cr.
13	59° 31′55.1″	26° 54′33.5″	115	83.5	219.5	1.6	309.7	6.31	0.57	219	1	15	9	Cr.
14	59° 29′37.6″	26° 55′30.3″	290	74.17	47.8	7.53	139.68	13.84	0.69	45	1	15	9	Cr.
15	59° 29′46.8″	26° 54′42.9″	56	87.15	92.85	−2.28	182.79	1.7	0.34	93	1	16	9	Cr.
16	59° 38′20.6″	26° 32′6.36″	44.1	1.23	134.9	33.5	312.2	56.4	0.318	224	3	14	8	Cr.
17	59° 38′18.8″	26° 28′50.4″	210	5.79	296	−31	309	58.3	0.661	28	3	11	8	Eo.
18	59° 58′23.2″	26° 30′6.72″	19.8	13.1	133.4	59.9	283.2	26.6	0.389	17	2	11	8	Eo.
19	59° 59′10.9″	26° 29′4.44″	219	33.1	246.4	−54	317.9	13.1	0.83	43	2	13	3	Eo.
20	59° 59′41.6″	26° 28′3.78″	186	10.8	273.8	−9	324.9	75.8	0.789	185	3	13	9	L.M
21	60° 33′26.2″	26° 44′09.4″	311	25.3	25.79	−29	75.16	50.1	0.33	304	3	11	9	Eo.
22	60° 33′37.6″	26° 42′06.1″	191	0.24	281.6	33.2	101.1	56.8	0.41	191	3	11	9	L.M
23	60° 42′03.7″	26° 40′52.5″	229	2.55	319.7	13.5	128.6	76.3	0.597	230	3	9	7	Eo.
24	60° 43′13.0″	26° 40′32.6″	220	31.6	306.2	−6.2	26.27	57.6	0.509	218	3	9	7	Eo.
25	60° 55′23.9″	26° 49′41.0″	41	0.25	131.1	24.5	310.4	65.4	0.753	221	3	10	6	Ol.
26	60° 57′14.3″	26° 56′48.4″	55.8	11.3	144.4	−6.7	204.2	76.8	0.744	235	3	16	9	Eo.
27	60° 57′40.9″	26° 56′43.4″	57.8	23.4	161.5	28.7	294.8	51.4	0.878	244	3	14	9	Eo.
28	60° 59′13.2″	26° 56′6.42″	38.2	9.06	138.9	49.4	300.7	39.2	0.845	223	3	14	10	Eo.
29	61° 01′35.2″	26° 54′2.88″	348	14.7	5.71	−75	79.63	4.34	0.143	349	2	11	6	Ol.
30	61° 01′41.5″	26° 53′43.0″	357	20.2	39.8	−64	93.54	16.4	0.779	180	2	13	7	Ol.
31	61° 14′38.6″	26° 36′28.3″	357	5.6	87.53	0.81	185.7	84.3	0.329	177	3	11	8	Ol.
32	61° 13′25.4″	26° 33′37.0″	14	19.2	104.8	2.3	201.4	70.7	0.561	15	3	11	7	Ol.
33	61° 18′02.9″	26° 23′25.8″	22.8	15.5	113.6	2.5	212.4	74.3	0.31	22	3	7	5	M.M.
34	61° 26′58.9″	26° 16′59.0″	221	5.97	309.5	−17	329.6	71.5	0.789	40	3	11	5	Ol.
35	61° 23′44.3″	26° 15′46.2″	349	23.4	87.01	17.9	210.8	59.8	0.937	173	3	15	9	Ol.
36	61° 23′03.3″	26° 15′40.0″	220	18.2	311.1	3.45	51.41	71.4	0.953	221	3	14	7	Ol.
37	61° 05′51.9″	26° 13′58.0″	27.4	22.7	120.2	6.75	225.8	66.2	0.756	209	3	12	7	Ol.
38	60° 20′47.5″	26° 18′26.1″	200	17.3	283.6	−18	330	64.3	0.855	197	3	15	9	Ol.
39	60° 20′22.4″	26° 18′31.9″	51.4	30.4	127.9	−22	188.4	51.2	0.493	224	3	12	8	Ol.
40	60° 21′58.8″	26° 19′06.9″	23.3	21.9	107.9	−13	169.2	64.1	0.814	201	3	14	9	Ol.
41	60° 21′46.0″	26° 19′36.1″	23.3	21.9	107.9	−13	169.2	64.1	0.814	201	3	11	9	Ol.
42	60° 34′27.8″	26° 32′03.8″	185	13	277.9	11.5	48.16	72.6	0.567	186	3	11	9	L.M.
43	60° 33′4.62″	26° 36′34.7″	207	39.6	321.9	27.1	75.85	38.5	0.343	221	3	11	7	Ol.
44	60° 03′22.6″	26° 25′39.4″	18.1	21.6	72.75	−56	118.9	25.4	0.438	24	2	15	10	L.M.

(continued)

Table 13.1 (continued)

Lab	Longitude-E	Latitude-N	S1.az	S1.pl	S2.az	S2.pl	S3.az	S3.pl	r0	Mahaz	SV	n	Exp	Str.
45	60° 02′55.9″	26° 26′17.6″	38.2	20.2	87.3	−61	136.1	20.3	0.986	222	2	9	6	L.M.
46	60° 05′9.6″	26° 21′20.6″	36.4	34.8	152.3	32.1	272.5	38.8	0.676	49	3	11	6	L.M.
47	59° 56′13.7″	26° 22′07.5″	23.4	7.56	117.2	26.2	278.6	62.5	0.586	26	3	12	11	Ol.
48	60° 10′19.8″	26° 16′25.0″	225	6.68	325.1	57.4	130.4	31.8	0.824	228	3	10	5	Ol.
49	59° 58′56.1″	26° 15′59.8″	38.4	43.6	126.9	−1.5	215.3	46.3	0.915	218	3	11	7	E.M.
50	60° 12′10.1″	26° 13′04.4″	326	10.9	50.13	−29	74.73	58.7	0.714	143	3	14	8	E.M.
51	59° 59′28.4″	26° 10′07.4″	34.5	32.1	132.4	12.4	240.7	55	0.621	218	3	10	7	E.M.
52	60° 58′22.4″	26° 04′31.7″	5.05	16.2	93.54	−5.2	166.2	73	0.832	185	3	21	17	M.M.
53	60° 58′22.7″	26° 03′27.5″	200	17.3	283.6	−18	330	64.3	0.855	196	3	8	6	M.M.
54	61° 31′52.7″	26° 05′28.5″	3.02	2.44	93.19	3.95	241.4	85.4	0.955	3	3	19	9	E.M.
55	60° 36′16.2″	25° 53′42.4″	3.02	2.44	93.19	3.95	241.4	85.4	0.955	3	3	12	8	M.M.
56	60° 26′27.9″	25° 38′23.2″	110.8	78.53	286.8	11.44	16.98	0.78	0.54	285	1	6	6	L.M.
57	60° 28′02.6″	25° 32′51.7″	164	77.1	291.9	8.09	23.35	10	0.756	112	1	9	7	L.M.
58	60° 18′10.0″	25° 21′11.4″	0.66	79.3	13.6	−10	103.2	2.33	0.729	14	1	5	4	L.M.
59	60° 40′30.8″	25° 15′27.5″	67.8	57	161.3	2.27	252.79	32.91	0.66	161	1	5	4	L.M.
60	61° 05′34.1″	26° 44′04.3″	8.36	20.43	145.2	62.96	271.86	16.93	0.83	5	2	6	5	L.M.
61	60° 28′54.6″	26° 41′38.3″	6.78	27.66	91.04	−10.97	161.2	60.26	0.757	184	3	10	9	Eo.
62	59° 47′31.4″	26° 19′00.6″	3.2	12.02	120.5	65.11	268.41	21.45	0.886	181	2	26	20	Ol.
63	60° 42′01.5″	26° 19′40.3″	199.4	12.68	288.0	−6.13	352.82	75.86	0.80	198	3	21	17	Ol.
64	59° 31′34.3″	26° 50′58.3″	123.1	2.86	213.2	3.28	352.13	85.64	0.44	303	3	10	7	Cr.

Lab label of site, *az* Azimuth; *pl* plunge, *Mahaz*, maximum horizontal stress axis, *SV* vertical stress axis, *n* number of measured fault data, *Exp* number of selected faults with angular error smaller than 30° from the calculated stress tensor, *Str* stratigraphic age of faulted rocks, *Cr* Cretaceous, *Eo* Eocene, *Ol* Oligocene, *E.M* Early Miocene, *M.M* Middle Miocene, *L.M* Late Miocene

random search trying 5,000 tensors, had to accept an angular error smaller than 30° for 60 % of the local fault-slip data. Any tensor obtained from less than 5 fault data was rejected. The 64 sites are those that yielded single tensors compatible with an adequate proportion of data. Data and geographic information about each accepted site are listed in Table 13.1.

Results

Most of the maximum principal stress directions ($\vec{S}_1$) plunge shallowly towards NNE or SSW (Fig. 13.10a). This nearly horizontal compression is consistent with the nearly E–W trend of regional folds, which suggests that folds and faults formed in the same stress field. Eight sites have yielded vertical to subvertical maximum principal stress (Fig. 13.10a and b), defining extension. Such orientations were expected since our measurement sites avoided regions where layers dip >20° and the fact that one principal stress is subvertical at some distance from major fault zones is a classical assumption (Anderson 1905).

The intermediate and minimum principal stress directions $\vec{S}_2$ and $\vec{S}_3$ scatter more than $\vec{S}_1$. Stereoplots of principal stresses and the triangular diagram of (Frohlich 1992) show few, yet not far from vertical principal stress directions (Fig. 13.10a and b). This could be due to minor fold- or fault-related rotation after the measured fault planes were activated by the calculated stress tensor. The tectonic regime plot (Fig. 13.10c) confirms two faulting regimes: (1) compression to transpression and (2) extension. The map of horizontal principal stress-directions (Fig. 13.3) was produced by projecting two of the principal stress axes $\vec{S}_1, \vec{S}_2$ or $\vec{S}_3$ onto the horizontal plane and so approximately fitting the Anderson assumption (Anderson 1905), for which one stress axis is vertical.

Compression and Transpression

Both compressional and transpressional regimes show sub-horizontal to shallow plunging (<30°) $\vec{S}_1$, in either NNE or SSW direction (Fig. 13.10a). Stress components $\vec{S}_2$ and $\vec{S}_3$ are scattered on a subvertical plane perpendicular to $\vec{S}_1$, (Fig. 13.10a). Site 40 and Site 8 are chosen to illustrate the compressional and transpressional tectonic regimes, respectively, because they are based on a large number of fault data and document the quality of the results.

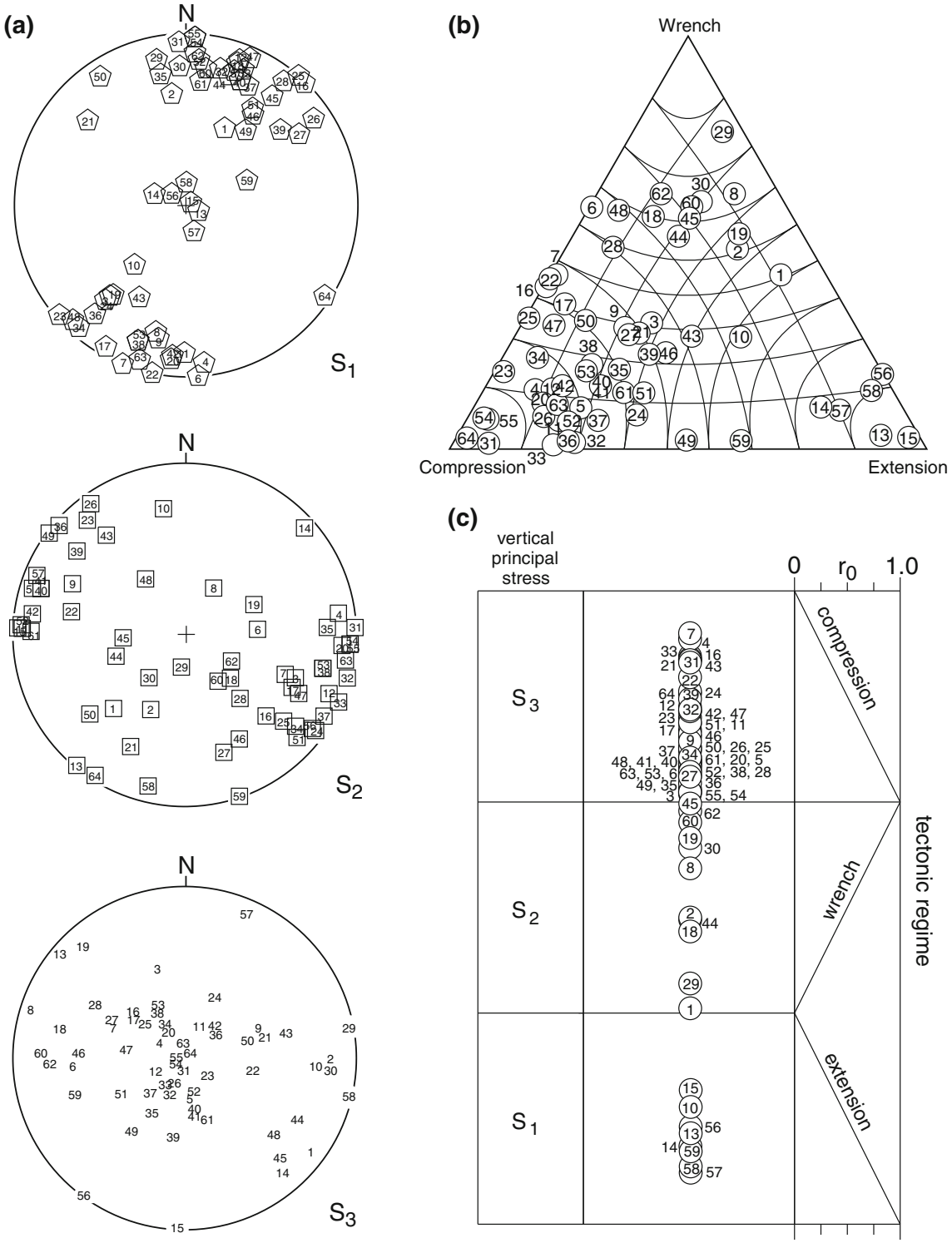

Fig. 13.10 Plots of the 64 stress tensors of sites listed in Table 13.1. **a** Equal area, lower-hemisphere projection of the principal stress axes $\vec{S}_1, \vec{S}_2$ and $\vec{S}_3$, **b** Triangular classification (Frohlich 1992) of stress axes, **c** Tectonic regime plot (Armijo et al. 1982; Philip 1987, Celerier 1995). $\vec{S}_1, \vec{S}_2$ and $\vec{S}_3$ are unit vectors with no magnitude; $r_0 = (\sigma_1 - \sigma_2)/(\sigma_1 - \sigma_3)$ where σ_i stands for principal stress magnitude

Compressional Tectonic Regime: Site 40

This site is in the direct hanging wall of the Ghasr Ghand Thrust, to the NE of Nikshahr. N- to NE-dipping reverse faults and conjugate S-dipping reverse faults are dominant (Fig. 13.11a). Nine out of fourteen measurements define the calculated paleostress tensor. This tensor has a NNW,

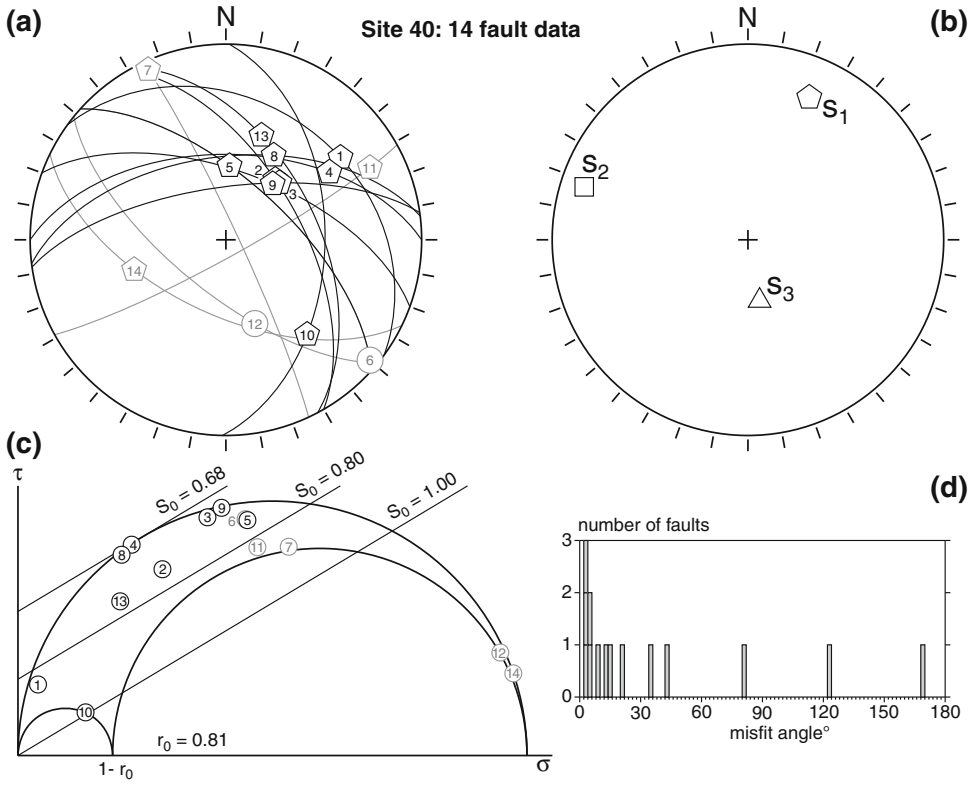

Fig. 13.11 Fault and tensor data of site 40 (location on Fig. 13.3). Stereographic, equal area lower hemisphere projections of **a** fault-slip data (*circles*: normal slip and pentagons: reverse slip); in *grey*, faults with misfit >30°. **b** Principal stress axes of the best tensor solution. **c** Mohr-diagram (explanation in text); *grey* faults as in **a**. **d** misfit plot (explanation in text). Data in Table 13.1

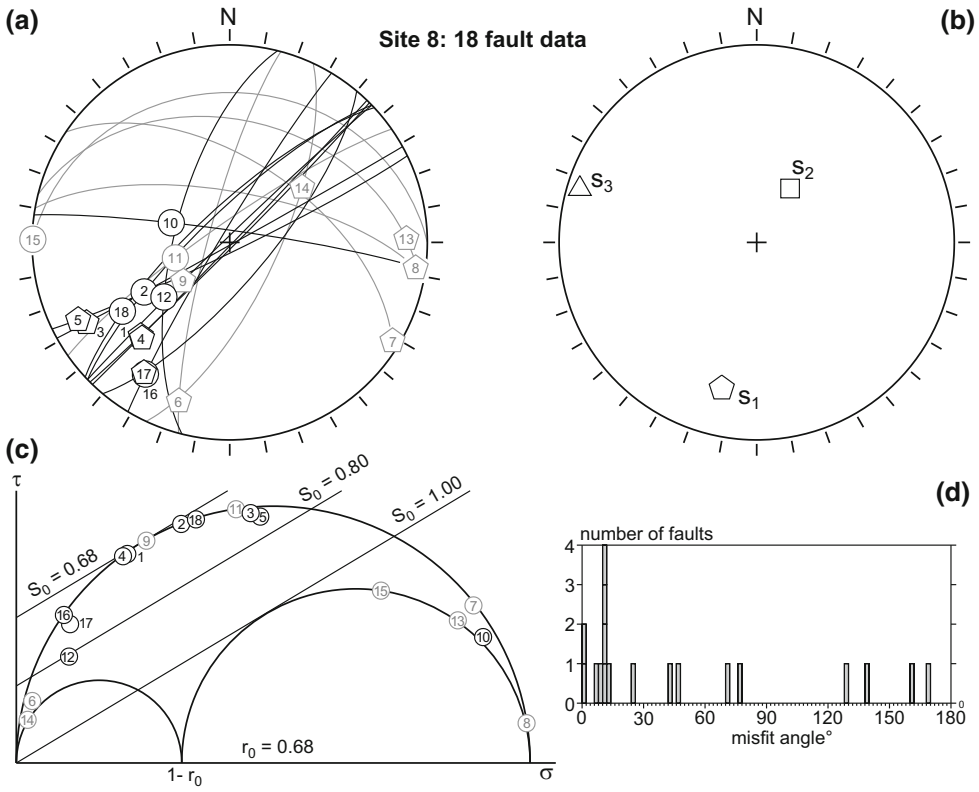

Fig. 13.12 Fault and tensor projections for site 8 (location Fig.13.3). Stereographic projections, Mohr-diagram and misfit plot as in Fig. 13.11. Data in Table 13.1

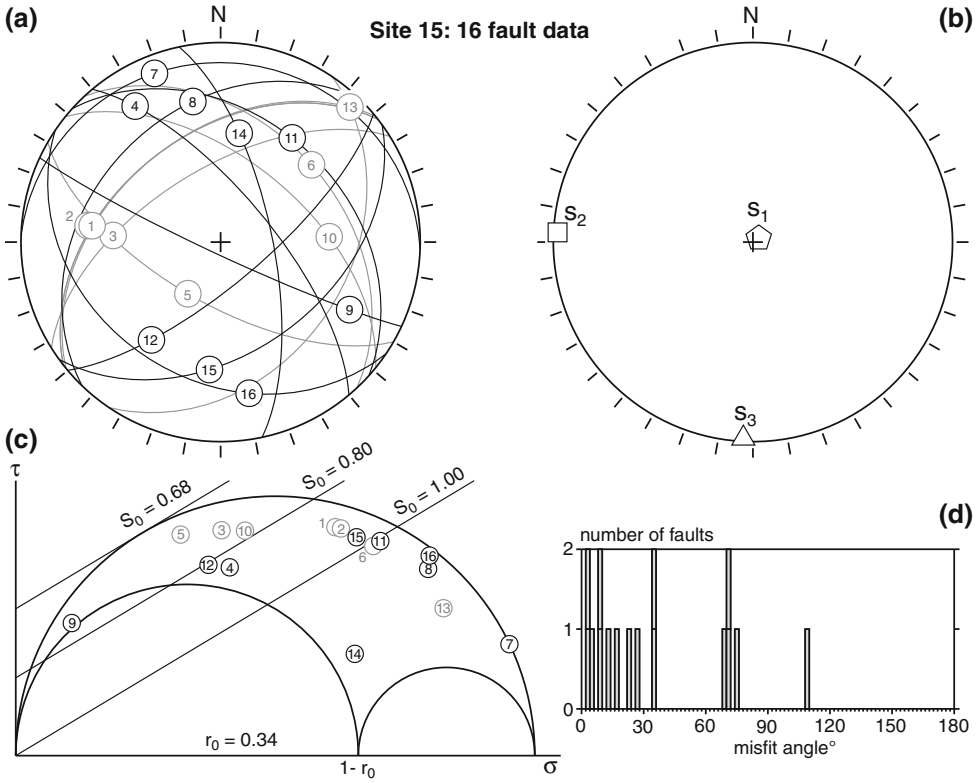

Fig. 13.13 Extensional stress tensor at site 15. Plot explanation in Fig. 13.11. Data in Table 13.1

subhorizontal maximum principal stress axis $\vec{S}_1$, and a subvertical minimum stress axis $\vec{S}_3$, (Fig. 13.11b). $\vec{S}_1$, is nearly perpendicular to the Ghasr Ghand Thrust zone (Fig. 13.3). A measure of how well the tensor explains the fault-slip data is given by the Mohr and angular misfit diagrams (Fig. 13.11c and d). The stress state of each fault is plotted in the Mohr circle representing the calculated stress tensor, along with the friction lines S_0. The slope of the friction line is defined by $S_0 = \mu/[\tau - \mu(\sigma_n - 1)]$, the required stress difference ratio to activate a fault plane. τ is shear stress and σ_n the normal stress computed from the reduced stress tensor ($S_0 = (\sigma_1 - \sigma_2)/^a1$ for a standard friction coefficient $\mu = 0.6$). Reactivation of the most favourably-oriented conjugate planes requires the stress difference to be above the threshold $S_c = 2\sin\varphi_0/1 + \sin\varphi_0$ with $S_0 \geq S_c$ and the friction angle $\varphi_0 = \arctan\mu$. Byerlee (1978) demonstrated that most rocks can be approximated with $\mu = 0.6$ and $\varphi_0 = 31°$, which yields $S_c = 0.68$. As S_0 increases above this threshold, the friction line cuts deeper and deeper into Mohr circles which means that more and more fault planes with unfavourable orientation can be reactivated. This process competes with the creation of new faults that become dominant for values $S0 \geq 0.8$ (Ohnaka 1973). Friction on favourably-oriented pre-existing faults actually limits the state of stress in the crust (Brace and Kohlstedt 1980), as in situ measurements tend to confirm (Zoback and Healy 1984). In site41, the

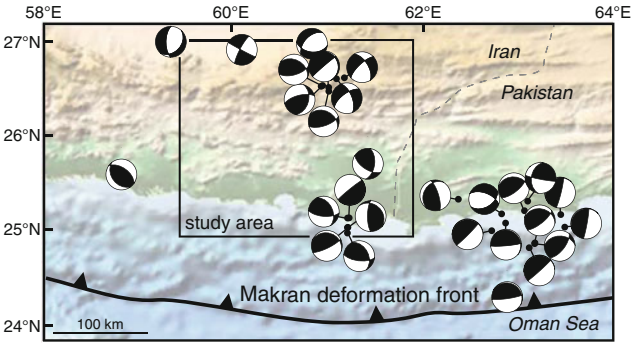

Fig. 13.14 Focal mechanisms in central MAW. References and data in Tables 13.2 and 13.3. Filled quadrants are compressional, empty quadrants are tensional

calculated stress tensor can activate 8 fault planes with a stress difference ratio $0.68 \leq S0 \leq 0.8$ (Fig. 13.11c). The misfit angle plot (Fig. 13.11d) shows that this tensor actually explains 9 faults with an angular error $< 30°$. One could argue that this number yields a poorly constrained tensor. Yet, comparison with the neighbouring sites 38 and 41, about 500 m away from site 40 supportively yield a comparable compression regime (Fig. 13.3 and Table 13.1). The r_0 value (0.81) indicates σ_2 being close to σ_3 . This difficult identification explains scattering of the calculated $\vec{S}_2$ and $\vec{S}_3$ in the plane perpendicular to $\vec{S}_1$. However, this site clearly records NNE–SSW compression.

Table 13.2 Earthquake focal mechanisms with defined P, B and T axes

n	Long (E)	Lat (N)	Depth (km)	*mb*	Paz	Ppl	Baz	Bpl	Taz	Tpl	Date
1	61.23	26.75	15	5.6	195	39	20	51	287	2	10.01.1979
2	61.31	26.75	15	5.6	184	36	22	52	280	9	10.01.1979
3	60.27	29.99	64	5.3	72	8	285	80	163	5	01.01.1980
4	58.86	25.59	15	5.7	43	8	311	8	177	78	07.12.1989
5	62.94	25.08	15	5.3	180	39	86	5	350	50	07.12.1991
6	62.88	24.25	15	5.6	177	36	83	6	345	53	30.01.1992
7	61.43	25.68	37	5.7	244	4	151	39	339	51	17.12.1992
8	60.91	27	72.4	5.3	89	73	259	17	350	3	24.06.2003

az azimuth and *pl* plunge. Data from Harvard CMT database

Table 13.3 Earthquake focal mechanisms with inferred fault plane based on preferred orientation relative to local tectonics

n	Long (E)	Lat (N)	Depth (km)	*MW*	*mb*	Strike	Dip	Rake	Date	References
1	63.48	26.15	27	7.9		246	7	89	27.11.1945	Byr
2	63.49	25.04	20	6.8		236	7	68	05.08.1947	Byr
3	60.95	26.55	3	5.8		256	61	13	10.01.1979	Byr
4	61.02	26.48	2	5.9		230	82	-4	10.01.1979	Byr
5	61.22	25.14	18	5.0		334	15	148	08.08.1972	Byr
6	62.87	25.19	26		4.7	290	49	-50	03.08.1968	Byr
7	62.75	24.99	18		5.1	279	9	84	13.02.1969	Byr
8	61.22	25.04	20		5.4	321	17	134	06.08.1972	Byr
9	61.22	25.14	18		5.4	334	15	148	08.08.1972	Byr
10	63.14	24.83	20		4.6	277	9	84	18.08.1972	Byr
11	63.21	24.88	18		5.2	281	23	70	02.09.1973	Byr
12	63.09	25.22	18		5.0	278	27	88	29.07.1975	Byr
13	62.40	25.33	18		5.1	214	16	19	10.02.1978	Byr
14	59.40	27.00	52		5.2	46	18	-90	29.05.1963	Ch
15	63.14	25.32	5		5.4	190	30	0	12.08.1963	Qu
16	61.22	25.04	33		5.5	292	22	114	06.08.1972	Ch
17	61.22	25.14	30		5.5	280	5	90	08.08.1972	Ch
18	63.21	24.88	30		5.3	270	30	90	02.09.1973	Qu
19	60.95	26.55	33		5.9	300	40	90	10.01.1979	JM
20	61.02	26.48	33		5.9	300	34	90	10.01.1979	JM

References: *Byr* (Byrne et al. 1992), *Ch* (Chandra 1984), *Qu* (Quittmeyer et al. 1984), *JM'* (Jackson and McKenzie 1984)

Transpressional Tectonic Regime: Site 8

The site is located in the boundary zone between the Jaz Murian depression and the Imbricate Zone, east of Espakeh. Ten out of 18 fault-slip data document subvertical NE–SW sinistral strike slip faults (Fig. 13.12a). The best-fit tensor obtained after inversion yields subhorizontal $\vec{S}_1$ and $\vec{S}_3$ shallowly plunging toward SSW and WNW, respectively, and a subvertical $\vec{S}_2$. (Fig. 13.12b). Ten faults have an angular error $< 30°$ (Fig. 13.12d). Nine of these ten faults can be activated by the calculated tensor with a stress difference ratio $0.68 \leq S_0 \leq 0.8$ (nine faults plot between the friction lines $S_0 = 0.68$ and $S_0 = 0.8$ in Fig. 13.12c). This site reveals a wrench tectonic regime with well-defined NNE–SSW-directed compression, hence transpression consistent with $r_0 = 0.68$.

Extension

Eight of the investigated sites yielded stress tensors with predominantly steep (>50°) stress components $\vec{S}_1$ indicative of an extensional regime (Fig. 13.10). This regime is dominant in Coastal Makran and less obvious further north up to the boundary of Jaz Murian (sites 10 and 13–15, Fig. 13.3). Both E–W and N–S extension directions were

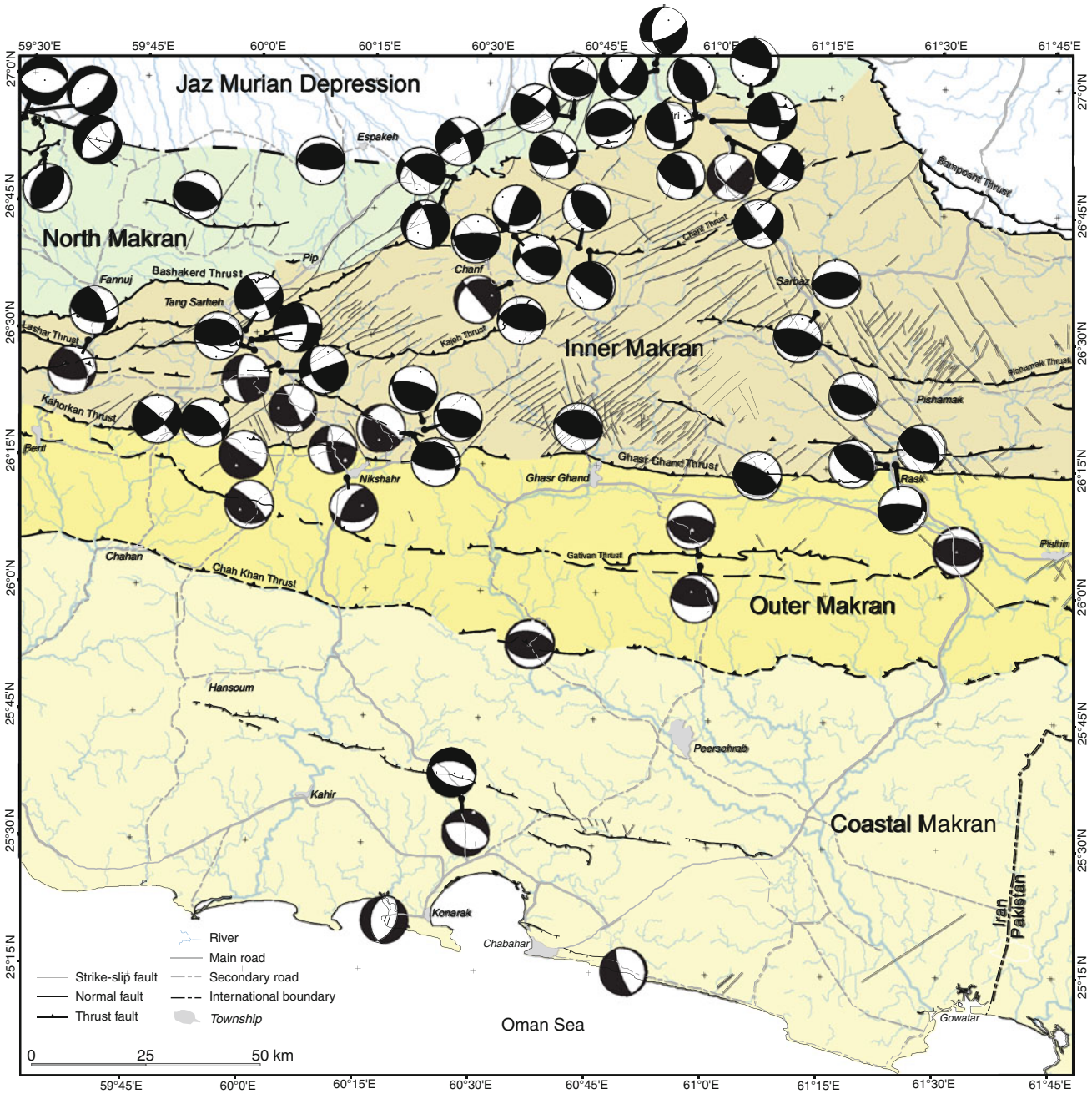

Fig. 13.15 Representation of calculated tensors in the form of focal mechanisms. Tensor data in Table 13.1. Compressional and extensional quadrants as in Fig. 13.14

found in Coastal Makran; mostly N–S extension was calculated along the Jaz Murian boundary. The well constrained site 15 is chosen to illustrate the extensional tectonic regime.

Extensional Tectonic Regime: Site 15

This site of sixteen fault measurements (Fig. 13.13a) is located in the contact zone between the Jaz Murian depression and the Imbricate Zone (Fig. 13.3). The best-fit tensor yields a vertical $\vec{S}_1$ and subhorizontal $\vec{S}_2$ and $\vec{S}_3$ which plunge toward W and S, respectively (Fig. 13.13b). The r_0 value of 0.34 implies a well-defined N–S extension direction.

Recent Stress Field

Earthquake focal mechanisms were used to constrain the present-day stress field (Fig. 13.14). Twenty-eight focal mechanisms (TableS 13.2 and 13.3), scattered over and around the study area, between longitude 58°E and 64°E

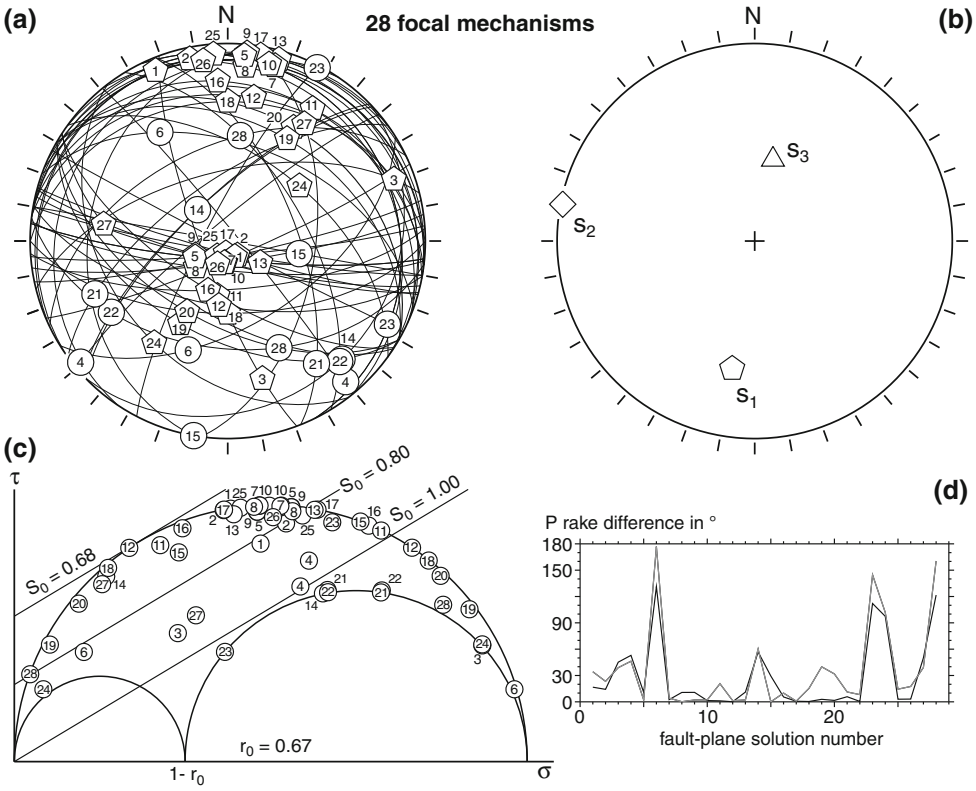

Fig. 13.16 Regional, present-day stress regime from inversion of focal mechanisms documented Fig. 13.14 and Tables 13.2 (numbers 21–28) and 3 (numbers 1–20) **a** Stereoplot of the nodal planes, **b** stereoplot of the best tensor for 70 % of the planes in **a** and **c** Mohr-diagram as in Fig. 13.11. Note that no preference is assigned to any nodal plane of the pair given for each focal mechanism. **d** Misfit plot of all nodal planes (1 *black* + 1 *grey* for each focal mechanism). The calculated tensor uses the best-fitting plane as active plane of each event. Note strong similarity between this tensor and that of site 8, Fig. 13.12

and latitude 24°N and 27°N, were gathered from the literature and world-wide-web data bases (Chandra 1984; Byrne et al. 1992; Jackson and McKenzie 1984; Quittmeyer et al. 1984 and Harvard CMT database). The premise is that the P, B and T axes of focal mechanisms provide an acceptable indication of the active principal stress directions with P axes replicating $\vec{S}_1$ and T axes $\vec{S}_3$ directions (Celerier 1999; Burg et al. 2005).

Focal mechanisms located in North-, Inner- and Outer Makran indicate nearly N–S compression, comparable with what was obtained from the fault analysis. Similarly, focal mechanisms on the boundary with the Jaz Murian depression indicate strike-slip faulting consistent with the calculated transpression. Focal mechanisms in Coastal and offshore Makran (mainly out of the study area) indicate active thrusting and strike-slip faulting, in contrast to the extension obtained from paleostress calculations. All earthquakes related to active compression have depths >18 km (Tables 13.2 and 13.3). The two earthquakes related to normal faulting (Table 13.3, numbers 6 and 15) occurred at 26 and 5 km depth. These relationships suggest that extension occurs in the higher crustal levels while compression is deep-seated, perhaps closely related to the subducting slab (Jacob and Quittmeyer 1979; Byrne et al. 1992; Engdahl et al. 2006).

To complement this work, the tensor map of the area can be extracted from the calculated tensors (Fig. 13.15) and compared with that of the earthquake focal mechanisms (Fig. 13.14). We first applied the stress inversion method to the 28 available data on focal mechanisms (Tables 13.2 and 13.3), which were all converted in terms of strike, rake and P-B-T axes (e.g. Angelier 2002; Lacombe et al. 2006). The technique assumes a uniform state of stress over the studied area and tests equally the two nodal planes of each focal mechanism. The result is a regional tensor whose shape characterizes a stress regime. We obtained NNE compression (Fig. 13.16) quite consistent with most calculations from fault-slip data. The plunge of the regional $\vec{S}_1$ (35° towards N190) might be a technical noise, since calculations take into account all planes and all focal mechanisms alike and ignore regional variations. We limited this data-smoothing effect with the best-fitting tensor for 70 % of all planes. From the directional and regime consistency between tensors from geological and seismic information, we decided to represent each fault-slip tensor in the form of pseudo-focal mechanisms. The caveat of this representation is in assuming that the stress axis $\vec{S}_1$ is parallel to the P-axis of crustal deformation, although these two axes may depart from each other (e.g. Twiss and Unruh 1998). Yet this representation didactically illustrates that these two types of interpretation yield matching information. It is worth noting that the extensional focal mechanisms in the Pakistani Coastal Makran (numbers 6 and 15 in Table 13.3) show radial extension like the calculated tensors in the Iranian Coastal Makran.

Discussion

The distribution and orientation of calculated paleostress tensors indicate regional NNE–SSW compression. This direction is coherent, whether measured in pre- or post olistostrome settings. This direction is also consistent with mapped fold trends and major thrusts (Ghasr Ghand, Gativan, Pishamak and Lashar) as well as with the present-day convergence direction between the Arabian and Iranian plates (e.g. Nilforoushan et al. 2003; Reilinger et al. 2006). This point shows that the structural development of MAW evolved under a stable stress field, at least for the last ca. 10 Ma. The calculated compression direction turns to NE–SW in the northeastern part of the study area. This change reflects either a regional change in the stress field, or an older faulting event since the related tensors were all obtained from faulted rocks older than Oligocene. In the latter case, this older compression direction could be related to the N–S Sistan Suture Zone, which is located next to the north of the study area (Fig. 13.1). We were not able to find sites with superimposed striations or a sufficient number of incompatible fault data to possibly yield a local second tensor and know whether this NE–SW compression is evidence for a change in space or time. More studies of the Sistan-Makran transition zone is necessary before any conclusion can be asserted.

Paleostress calculations additionally substantiate the relative importance of wrenching and thrusting in North- and Inner Makran. r_0 values strongly depend on differential stress. Since the vertical principal stress is essentially the lithostatic pressure, it reflects the thickness of overlying sediments. r_0 close to 1 (>0.80) for both compressional and transpressional regimes suggest shallow burial at the time of faulting.

NNE–SSW shortening deduced from conjugate strike-slip faults along the NE–SW Jaz Murian boundary contrasts with radial to N–S extension along the E–W segment of this boundary (site15, Fig. 13.3 and Table 13.1). This discrepancy suggests different faulting events whose time relationship could not be constrained by overprinting striation relationships. In places like site 10, to the east of Espakeh, NE–SW-striking sinistral faults turn to nearly N–S strikes. This directional change defines releasing bends of the strike slip faults, which are compatible with coeval transpression and local extension. Coastal Makran contains well defined N–S extension with r_0 values of 0.5–0.6 that suggest prolate shapes of the stress ellipsoid with a vertical σ_1. Near the coast, extension is nearly E–W with rather large (0.66–0.73) r_0 values. Since σ_2 and σ_3 are almost equal, extension is sub-radial and therefore has a weakly defined direction. This tectonic regime is regional since normal faults also exist in the Pakistani Makran (e.g. Cappel and Francis 1984). Planar and bookshelf geometries with few meter displacements along individual faults indicate near surface faulting. However, off-shore seismic profiles exhibit large listric normal faults in addition to smaller, planar normal faults (e.g.Grando and McClay 2007). Some authors (e.g. Kopp Fruehn et al. 2000; Grando and McClay 2007) suggested that underplating caused uplift and extension in coastal and off-shore Makran. This hypothesis would imply that normal faulting is widely distributed over the thick and eroded parts of the accretionary complex. This is not the case in the Iranian Makran where Plio-Pleistocene normal faults are restricted to the coastal region and are nearly absent further onshore. The significance of this extensional faulting requires additional data to be placed in the frame of the MAW.

Conclusion

This study is the first paleostress analysis in the Makran Accretionary Wedge. It shows that the regionally distributed and dominant compressional to tranpressional regimes are consistent with the orientation of folds, thrusts and strike-slip faults in all lithologies, from the Cretaceous to the Upper Miocene. NNE–SSW compression is also consistent with the active stress field obtained from earthquake focal mechanisms. We conclude that the structural development of MAW evolved under a quite stable stress field for at least 10 Ma, with a compression direction close to the direction of convergence between the Arabian and Iranian plates (e.g. Vernant et al. 2004). The NE compression in the north-eastern part of the study area occurs in the transition zone between the E–W MAW and N–S Sistan Suture Zone and might reflect stress deviation in the interference zone.

Extension characterizes a more complex and timely less stable system. Local extensional events recorded along the Makran-Jaz Murian boundary are related to releasing bends of strike-slip faults. Coastal Makran registered regional, radial extension whose significance is still unclear (variation in subduction geometry or rate, collapse of the active wedge?). Our field observation and seismic data from off-shore Makran (e.g. Ellouz-Zimmermann et al. 2007; Grando and McClay 2007) indicate the activity of normal faults during Pleistocene to present times.

The excellent fit between calculated stress tensors and focal mechanisms data should help predicting the types of earthquakes one may have to face in the region.

Acknowledgements The Swiss National Fond supported this work (project 2-77 634-05). Financial contribution and support from the MEBE program and the Geological Survey of Iran are also acknowledged. Sincere thanks are extended to the many people who hosted and helped us in the remote places of the Makran. We are indebted to B. Celerier for guidance on the inversion program and to D. Bernoulli and

J. Smit for useful discussions in the field. Reviews by D. Frizon de Lamotte and O. Lacombe helped to significantly improve our presentation. We thank the editor, F. Roure, for his useful comments and for offering the opportunity to publish these results.

References

Alinaghi A, Koulakov I, Thybo H (2007) Seismic tomographic imaging of P- and S-waves velocity perturbations in the upper mantle beneath Iran. Geophys J Int 169(3):1089–1102. doi: 10.1111/j.1365-246X.2007.03317.xI

Anderson EM (1905) The dynamics of faulting. Trans Edinb Geol Soc 8:387–402

Angelier J (1984) Tectonic analysis of fault slip data sets. J Geophys Res 89(B7):5835–5848. doi: 10.1029/JB089iB07p05835I

Angelier J (1994) Fault slip analysis and paleostress reconstruction. In: Continental deformation. Oxford, Pergamon press Ltd.: 53–100

Angelier J (2002) Inversion of earthquake focal mechanisms to obtain the seismotectonic stress IV—a new method free of choice among nodal planes. Geophys J Int 150(3):588–609. doi: 10.1046/j.1365-246X.2002.01713.xI

Armijo R, Carey E, Cisternas A (1982) The inverse problem in microtectonics and the separation of tectonic phases. Tectonophysics 82(1–2):145–160. doi:10.1016/0040-1951(82)90092-0I

Bijwaard H, Spakman W, Engdahl ER (1998) Closing the gap between regional and global travel time tomography. J Geophys Res 103(B12):55–78. doi:10.1029/98JB02467I

Bird P, Toksoz MN, Sleep NH (1975) Thermal and mechanical models of continent-continent convergence zones. J Geophys Res 80(32):4405–4416. doi:10.1029/JB080i032p04405I

Bott MHP (1959) The mechanics of oblique slip faulting. Geol Mag 96:109–117

Brace WF, Kohlstedt DT (1980) Limits on lithospheric stress imposed by laboratory experiments. J Geophys Res 85(B11):6248–6252. doi: 10.1029/JB085iB11p06248I

Burg J-P, Celerier B, Chaudhry MN, Ghazanfar M, Gnehm F, Schnellmann M (2005) Fault analysis and paleostress evolution in large strain regions: methodological and geological discussion of the southeastern himalayan fold-and-thrust belt in Pakistan. J Asian Earth Sci 24(4):445–467. doi:10.1016/j.jseaes.2003.12.008I

Burg J-P, Bernoulli D, Smit J, Dolati A, Bahroudi A (2008) A giant catastrophic mud-and-debris flow in the Miocene Makran. Terra Nova 20(3):188–193

Byerlee JD (1978) Friction of rocks. Pure Appl Geophys 116 (4/5):615–626

Byrne DE, Sykes LR, Davis DM (1992) Great thrust earthquakes and aseismic slip along the plate boundary of the Makran Subduction Zone. J Geophys Res 97(B1):449–478. doi: 10.1029/91JB02165I

Celerier B (1995) Tectonic regime and slip orientation of reactivated faults. Geophys J Int 121(1):143–161. doi:10.1111/j.1365-246X.1995.tb03517.xI

Celerier B (1999) Fault slip analysis software. http://www.isteem.univ-montp2.fr/PERSO/celerier/software/software.bc.html

Chandra U (1984) Focal mechanism solutions for earthquakes in Iran. Phys Earth Planet Inter 34(1–2):9–16

Dercourt J, Zonenshain, LP, Ricou, LE, Kazmin VG, Le Pichon X, Knipper AL, Grandjacquet C, Sbortshikov IM, Geyssant J, Lepvrier C, Pechersky DH, Boulin J, Sibuet JC, Savostin LA, Sorokhtin O, Westphal M, Bazhenov ML, Lauer JP, Biju-Duval B (1986) Geological evolution of the tethys belt from the atlantic to the pamirs since the LIAS. Tectonophysics 123(1-4):241–315. doi: 10.1016/0040-1951(86)90199-XI

Dolati A (2010) Stratigraphy, structure geology and low-temperature thermochronology across the Makran accretionary wedge in Iran. PhD. thesis, ETH Zurich

Dupin J-M, Sassi W, Angelier J (1993) Homogeneous stress hypothesis and actual fault slip: a distinct element analysis. J Struct Geol 15(8):1033–1043

Ellouz-Zimmermann N, Lallemant SJ, Castilla R, Mouchot N, Leturmy P, Battani A, Buret C, Cherel L, Desaubliaux G, Deville E, Ferrand J, Lugcke A, Mahieux G, Mascle G, Miihr P, Pierson-Wickmann A-C, Robion P, Schmitz J, Danish M, Hasany S, Shahzad A, Tabreez A (2007) Offshore frontal part of the makran accretionary prism (Pakistan): the chamak survey. In: Lacombe O, Lave J, Roure F, Verges J (eds). Thrust belts and foreland basins: from fold kinematics to hydrocarbon systems. Springer, Berlin, pp 351–366

Engdahl ER, Jackson JA, Myers SC, Bergman EA, Priestley K (2006) Relocation and assessment of seismicity in the Iran region. Geophys J Int 167(2):761–778. doi:10.1111/j.1365-246X.2006.03127.xI

Etchecopar A, Vasseur G, Daignieres M (1981) An inverse problem in microtectonics for the determination of stress tensors from fault striation analysis. J Struct Geol 3(1):51–65

Frohlich C (1992) Triangle diagrams: ternary graphs to display similarity and diversity of earthquake focal mechanisms. Phys Earth Planet Int 75(1–3):193–198

Grando G, McClay K (2007) Morphotectonics domains and structural styles in the Makran accretionary prism, offshore Iran. Sediment Geol 196(1–4):157–179. doi:101016/jsedgeo200605030I

Hafkenscheid E, Wortel MJR, Spakman W (2006) Subduction history of the Tethyan region derived from seismic tomography and tectonic reconstructions. J Geophys Res 111(B08401). doi: 10.1029/2005JB003791

Harms JC, Cappel HN, Francis DC (1984) The Makran coast of Pakistan; its stratigraphy and hydrocarbon potential. In: Haq Bilal U, Milliman John D(eds). Marine geology and oceanography of Arabian Sea and coastal Pakistan. Van Nostrand Reinhold Co., New York, NY, United States, pp 3–l26

Hosseini-Barzi M, Talbot CJ (2003) A tectonic pulse in the Makran accretionary prism recorded in Iranian coastal sediments. J Geol Soc London 160:903–910

Jackson J, McKenzie D (1984) Active tectonics of the Alpine-Himalayan belt between western Turkey and Pakistan. Geophys J Roy Astron Soc 77(1):185–264

Jacob KH, Quittmeyer RL (1979) The Makran region of Pakistan and Iran: Trench-arc system with active plate subduction. In: Farah A,de Jong KA(eds). Geodynamics of Pakistan, Quetta, Pakistan, pp 305–317

Kopp C, Fruehn J, Flueh ER, Reichert C, Kukowski N, Bialas J, Klaeschen D (2000) Structure of the Makran subduction zone from wide-angle and reflection seismic data. In: Carbonell R, Gallart J, Torne M (eds). Deep seismic profiling of the continents and their margins. Elsevier, Amsterdam, Netherlands 2000

Lacombe O, Mouthereau F, Kargar S, Meyer B (2006) Late Cenozoic and modern stress fields in the western Fars (Iran): implications for the tectonic and kinematic evolution of central Zagros Tectonics 25: TC1003. doi: 10.1029/2005TC001831I

McCall GJH, Kidd RGW (1982) The Makran, southeastern Iran; the anatomy of a convergent plate margin active from Cretaceous to present. In: Leggett Jeremy K (ed). Trench-Forearc geology; sedimentation and tectonics on modern and ancient active plate margins, conference. Special publication—geological society of London 10. Geological society of London, London, United Kingdom, pp 387–397

McClay KR (1992) Thrust tectonics. Chapman and Hall, London

Molnar P, Stock JM (2009) Slowing of India's convergence with Eurasia since 20 Ma and its implications for Tibetan mantle dynamics. Tectonics 28: TC3001. doi: 10.1029/2008TC002271I

Nilforoushan F, Masson F, Vernant P, Vigny C, Martinod J, Abbassi M, Nankali H, Hatzfeld D, Bayer R, Tavakoli F, Ashtiani A, Doerflinger E, Daignieres M, Collard P, Chery J (2003) GPS network monitors the Arabia-Eurasia collision deformation in Iran. J Geod 77(7–8):411–422

Ohnaka M (1973) The quantitative effect of hydrostatic confining pressure on the compressive strength of crystalline rocks. J Phys Earth 21:125–140

Paul J, Burgmann R, Gaur VK, Bilham R, Larson KM, Ananda MB, Jade SMM, Anupama TS, Satyal G, Kumar D (2001) The motion and active deformation of India. Geophys Res Lett 28(4):647–651. doi:10.1029/2000GL011832I

Petit J-P (1987) Criteria for the sense of movement on fault surfaces in brittle rocks. J Struct Geol 9(5–6):597–608

Philip H (1987) Plio-Quaternary evolution of the stress field in Mediterranean zones of subduction and collision. Ann Geophys 5B:301–320

Platt JP, Leggett JK, Young J, Raza H, Alam S (1985) Large-scale sediment underplating in the Makran accretionary prism. Southwest Pakistan Geol 13(7):507–511. doi:101130/0091-7613(1985)13<507:LSUITM>20CO;2I

Quittmeyer RC, Kafka AL, Armbruster JC (1984) Focal mechanisms and depths of earthquakes in central Pakistan; a tectonic interpretation. J Geophys Res 9(B4):2459–2470. doi: 10.1029/JB089iB04p02459I

Reilinger R, McClusky S, Vernant P, Lawrence S, Ergintav S, Cakmak R, Ozener H, Kadirov F, Guliev I, Stepanyan R, Nadariya M, Hahubia G, Mahmoud SK, Sakr K, ArRajehi A, Paradissis D, Al-Aydrus A, Prilepin M, Guseva T, Evren E, Dmitrotsa A, Filikov SV, Gomez F, Al-Ghazzi R, Karam G (2006) GPS constraints on continental deformation in the Africa-Arabia-Eurasia continental collision zone and implications for the dynamics of plate interactions. J Geophys Res 111(B05411). doi:10.1029/2005JB004051

Stoecklin J (1968) Structural history and tectonics of Iran; a review. Am Assoc Petrol Geol Bull 52(7):1220–1258

Stoneley R (1974) Evolution of the continental margins bounding a former southern Tethys. In: Burk CA, Drake CL(eds). The geology of continental margins. Springer,Berlin, pp 889–903

Twiss RJ, Unruh JR (1998) Analysis of fault slip inversions: do they constrain stress or strain rate? J Geophys Res 103:12205–12222. doi:10.1029/98JB00612I

Vernant P, Nilforoushan F, Hatzfeld D, Abbassi MR, Vigny C, Masson F, Nankali H, Martinod J, Ashtiani A, Bayer R, Tavakoli F, Chery J (2004) Present-day crustal deformation and plate kinematics in the Middle East constrained by GPS measurements in Iran and northern Oman. Geophys J Int 157(1):381–398. doi: 10.1111/j.1365-246X.2004.02222.xI

Wallace RE (1951) Geometry of shearing stress and relation to faulting. J Geol 59:118–130

White RS, Klitgord K (1976) Sediment deformation and plate tectonics in the Gulf of Oman. Earth Planet Sci Lett 32(2):199–209

White RS, Louden KE (1982) The Makran continental margin; structure of a thickly sedimented convergent plate boundary. In: JS W, CL D(eds). Studies in continental margin geology. AAPG Memoir 34. American Association of Petroleum Geologists, Tulsa,OK, United States, pp 499–518

Zoback MD, Healy JH (1984) Friction, faulting, and in situ stress. Ann Geophys 2:689–698